24/04/2024 23:28

(Article begins on next page)

Melting below Mid Ocean Ridges: thermal effects of pyroxenites in the peridotitic mantle

Daniele Brunelli[1,2*], Anna Cipriani[1,3*], Enrico Bonatti[2,3]

[1] Dipartimento di Scienze Chimiche e Geologiche, Università di Modena e Reggio Emilia, Via Campi 103, 41125 Modena, Italy.

[2] Istituto di Scienze Marine, CNR, Via Gobetti 101, 40129 Bologna, Italy.

[3] Lamont Doherty Earth Observatory, Columbia University, Palisades, New York 10964, USA.

* Corresponding authors: *daniele.brunelli@unimore.it; anna.cipriani@unimore.it*

After travelling in the Earth's interior for up to billions of years, recycled material once injected at subduction zones can reach a subridge melting region as pyroxenite dispersed in the host peridotitic mantle. We studied genetically related crustal basalts and mantle peridotites sampled along an uplifted lithospheric section created at a segment of the Mid Atlantic Ridge through a time interval of 26 Ma. The arrival of low-solidus material into the melting region forces the elemental and isotopic imprint of the residual peridotites and of the basalts to diverge with time. We show that a pyroxenite-bearing source entering the subridge melting region induces undercooling of the host peridotitic mantle, due to subtraction of latent heat by melting of the low-T solidus pyroxenite. Mantle undercooling in turn lowers the thermal boundary layer leading to a deeper cessation of melting. A consequence is to decrease the total amount of extracted melt, hence magmatic crustal thickness. The degree of melting undergone by a homogeneous peridotitic mantle is higher than the degree of melting of the same peridotite but veined by pyroxenites. This effect, thermodynamically predicted for a marble-cake type peridotite-pyroxenite mixed source, implies incomplete homogenisation of recycled material in the convective mantle.

29

Mantle rising beneath the 60,000 km long Mid Oceanic Ridge system contains, as in a slow-motion movie, a record of ancient upwelling and melting events and of interaction with subduction or hot spot-derived components. It is difficult to reconstruct temporal records of these ancient events due to lack of suitable samples; however, we were given the opportunity to explore the temporal evolution of the oceanic lithosphere composition and structure at 11°N along the Mid Atlantic Ridge (MAR) where an uplifted > 300 km long sliver of lithosphere exposes a basal mantle peridotite unit, lower crustal gabbros, a dyke complex and erupted basalts[1–3]. This lithospheric section (Vema Lithospheric Section or VLS) was generated at an 80 km long segment of the MAR (EMAR segment, Supplementary Fig. S1) during a 26 Ma time interval[1,2,4–6]. Both crustal basalts and their mantle peridotite parents have been densely sampled at the VLS along a seafloor spreading flow line[4] allowing comparisons of their isotopic and elemental composition throughout the 26 Ma time interval[1,2,4–6] (Fig. 1) .

Surprisingly, temporal variations of mantle degree of melting estimated from basalt Na_8[7,8] anti-correlate with the degree of melting derived from spinel Cr# of the peridotites[9,10], although the two curves converge to a common value in the youngest 3 Ma stretch of the VLS (Fig. 1). Older, isotopically enriched basalts display the lower Na_8 values of the entire VLS, suggesting they were generated by a higher degree of melting of their mantle source; in contrast, the genetically associated mantle peridotites record a relatively low extent of melting, in agreement with a thinner crust recorded by geophysical data[1]. This anti-correlation contrasts with what is inferred to be the "normal" signature of partial melting at mid-ocean ridges.

    We offer a solution to this conundrum by suggesting that a subridge variably veined mantle hosts chemically enriched, fertile, low-T melting components, i.e. pyroxenites. Thermodynamic-based studies predict dramatic effects when pyroxenites are present in the mantle source and partially melt along a decompressive path[11–15]. Low-T solidus components lower the extent of melting of the host peridotite due to subtraction of latent heat of fusion[13–15]. Pyroxenites melt preferentially, generating isotopically enriched, low Na_8 melts and cooling the host mantle peridotites, thereby lowering the degree of melting of the peridotite mantle in proportion to its pyroxenite content[13]. In this work we account for variable extents of the melting column by assuming that different pyroxenitic contents

61   result in variable extent of undercooling before the ambient peridotite starts melting. This

62   situation mimics varying the potential temperature of the mantle resulting in changes in the

63   length of the melting column.

64

65

66   Temporal variability of crustal thickness and mantle degree of melting

67

68   Basalt Nd, Sr and Pb isotopes vary coherently along the 26 Ma-long VLS section,

69   showing a decrease in isotopic enrichment towards younger ages that hints at temporal

70   variations of composition and thermal state of the rising mantle[8]. We represent these

71   variations as discrete steps (Fig. 1a), defining three time domains: 0-2 Ma, 2-13 Ma and

72   13-26 Ma (Supplementary Tables S1-S3).

73   The basalts major element composition also varies with age, the older samples being

74   poorer in sodium than the younger ones. Na_8, an inverse proxy of the degree of melting

75   experienced by the mantle column[7,8] (Supplementary Table S2), is on average lower in the

76   VLS older basalts; thus, they were apparently produced by a degree of melting higher than

77   the younger basalts (Supplementary Fig. S1a). However, Na_8 has been defined for a

78   homogeneous lherzolitic source[8]. A heterogeneous source generates complex melt mixing

79   patterns depending on the relative extent of melting, homogenisation and enrichment of

80   each component[16–18]. For this reason we adopt here the expression "apparent" degree of

81   melting.

82   The proxy equivalent (but reverse) to basalt Na_8 is in peridotites the Cr#

83   (Cr#=Cr/(Cr+Al)) of spinels and pyroxenes[9,10]. During the last 26 Ma, peridotite spinel

84   Cr# increased along the VLS on average from 22 to 37 (Supplementary Fig S1c)

85   suggesting that the amount of magma delivered at ridge axis increased through time, in

86   agreement with gravity profiles running along spreading-flow-lines (Supplementary Fig.

87   S1c), revealing that crustal thickness increased from 4.8±0.2 km in the 22-27 Ma interval

88   to 5.4±0.2 km between 0-5 Ma [1,4].

89   Based on calibrations of Warren, 2016[19], the degree of melting (F_{max}) of the VLS

90   peridotites increased from 8.0 to 14.2 F% toward younger crustal ages (average 10.8, Fig.

91   2). MORB glasses Na_8 increased with time along the VLS from 2.6 to 3.0 on average

92   (Supplementary Fig. S1a). F_{max} in the basalts can be estimated according to[7] and compared

93   to the F_{max} of the mantle peridotites. Comparing temporal sections of mantle residua and of

94   their melt products must take into account a time-delay in the emplacement of the mantle

95   peridotites in the oceanic crust. According to[1,4] we corrected the crustal ages of the mantle

96   rocks relative to that of basalts by a relative time lag of 2.2 Ma (see online Methods: Age

97   Correction).

98   The calculated apparent F_{max} of MORB glasses vary little during the 26 Ma-long VLS

99   stretch (Fig. 1b) with values ranging from 18.0 to 15.8 F% (ave. 16.7), significantly higher

100   than those estimated from mantle residual peridotites (Fig. 1b). A striking feature of the

101   Na_8 degree of melting curve is the decrease of the apparent F_{max} through time that

102   countertrends with both the associated mantle peridotites degree of melting curve and the

103   gravity-inferred crustal thickness (Fig. 1b; Supplementary Fig. S1c).

104

105   Significance of the decoupling

106

107   The degrees of melting estimated from the mantle peridotites and from the basalts can

108   be generated by variations of mantle potential temperature, mantle composition and

109   spreading rate. Changes in mantle temperature or source fertility will result in coherent

110   changes of the degrees of melting estimated from basalts and from peridotites. Similarly,

111   changes in spreading rate cannot decouple the behaviour of residual mantle and extracted

112   basalts, because, in a passive upwelling scenario, decreasing the spreading rate lowers the

113   thermal state of the entire melting region, and vice versa[20]. During the last 26 Ma the half

114   spreading rate at the EMAR segment decreased from 17.2 mm/a (Chron 6) to 16.9 mm/a

115   (Chron 5) to present-day 13.6 mm/a[21,22] (Supplementary Fig. S1b). Such decrease of

116   spreading rate toward younger ages should lower the mantle degree of melting by about

117   1%[20]; thus, the increase in degree of melting recorded by the VLS mantle peridotites must

118   be caused by processes other than changes in spreading rate, mantle temperature or

119   fertility.

120   We consider now a heterogeneous mantle source. Thermodynamic modelling of

121   melting a two-component mantle source predicts that when a fertile heterogeneity, i.e.

122   pyroxenite, starts melting, the temperature of the whole mantle parcel is lowered due to the

123   latent heat of melting[15]. If the heterogeneity is less than a few kilometres, some heat is

124   transferred from the peridotite into the melting heterogeneity increasing its melt

125   productivity while cooling the surrounding mantle[13–15]. Accordingly, the vertical interval

126   where only pyroxenites undergo melting represents an undercooling region whose extent is

127   proportional to the amount of pyroxenites (Fig. 2). It follows that, for a given P-T

128   decompression path, the degree of melting undergone by a homogeneous peridotitic

4

129   mantle is higher than the degree of melting of the same peridotite but veined by

130   pyroxenites.

131   A lithologically homogeneous mantle source, resulting in coherent estimates of the

132   degree of melting between peridotites and basalt proxies, is approximated in the younger

133   (< 5 Ma) portion of the VLS where both basalt- and peridotite-derived F% converge

134   toward a common value. We assume that the present-day subridge mantle (Vema

135   Unveined Mantle or VUM) contains negligible amounts of pyroxenites, not sufficient to

136   perturb thermally the melting process of the host mantle peridotite. Thus, for this region

137   the Na_8-derived degree of melting is in line with its original interpretation[7,8,23].

138   In contrast, in a veined mantle scenario, degrees of melting estimated from peridotites

139   and from basalts differ strongly. While the Cr# records the true F_{max} of the ambient

140   peridotite, the pooled melts aggregate the compositional signal of both (low F) peridotitic

141   and (high F) pyroxenitic melts[18]. We propose that the low degree of melting of the older

142   portion of the VLS peridotites is due to heat consumption during preferential melting of a

143   pyroxenitic component at nearly constant mantle potential temperature. Along the VLS we

144   have decreasing quantities of pyroxenites injected into the melting region, with consequent

145   decrease of the undercooling effect and expansion of the anhydrous peridotite melting

146   region.

147   We tested this hypothesis by modelling the decompressive adiabatic melting of a mixed

148   source based on the experimental-parameterized algorithm Melt-PX[24]. Mantle potential

149   temperatures have been constrained using the passive flow temperature field model of

150   Bonatti et al., (2003)[1] giving a mantle Tp = 1350 °C. For this temperature and a lherzolitic

151   source containing 15% clinopyroxene, Melt-PX calculations overestimate crustal thickness

152   and mantle degrees of melting observed at the EMAR segment (Fig. 3). These calculations

153   assume that melting ceases at the base of the crust, a boundary condition acceptable for

154   high mantle Tp settings as in fast spreading ridges or hotspots[24,25]. They represent the

155   model maximum allowed thickness at a given thermal setting (Fig. 3). Mantle flow

156   models[1,26] predict the end of melting to occur at $P_f \approx 0.7$ GPa, well below the base of the

157   crust. This condition applies to low-spreading ridges due to heat conduction to the surface

158   resulting in a deep transition from the conductive to the convective thermal region[20,26–28].

159   As low-melting component we adopted the silica deficient pyroxenite M7-16[29] for

160   reasons defined in the next section. We observe that an increase in the fraction X_p of

161   pyroxenite in the mantle is paralleled by a decrease of degree of melting of the host

162   peridotite (F_π) (Fig. 3) depending also on the final pressure of melting (varying in the

163   range 0.3-1.1 GPa, Fig. 3).

164   Integration of the melt productivity of the host peridotite and of the pyroxenite along an

165   adiabatic path, weighted by their relative abundance, allows estimating magmatic crustal

166   thickness. Lambart et al., (2016)[24] show that the total magmatic productivity increases

167   proportionally to the amount of pyroxenite in the source. This observation apparently is in

168   contrast with the increase toward younger ages along the VLS of gravity-inferred crustal

169   thickness, paralleled by a decrease of the estimated amount of pyroxenites dispersed within

170   the mantle (Fig. 2, Supplementary Fig. S1c). This contradiction is solved considering that

171   increasing the amount of low-melting lithologies enhances the undercooling of the host

172   peridotitic mantle due to heat diffusion into the melting pyroxenite[13]. Undercooling

173   estimated by Melt-PX calculations can reach up to 40 °C for adiabatic melting under the

174   assumed conditions. Reduced undercooling due to a decrease of the mantle pyroxenite

175   fraction during melting results in shallowing the final pressure of melting from $\approx$ 1.1 to 0.7

176   GPa going from the oldest to the youngest VLS sectors (Fig. 3, right panel).

177   These observations and numerical experiments reveal that in slow-spreading ridges, at

178   constant mantle potential temperature, the arrival of a pulse of pyroxenites in the mantle

179   source region will cause a reduction of crustal thickness. The countertrend of crustal

180   thickness and degree of mantle melting with spreading rate along the VLS is a positive test

181   of our hypothesis.

182

183

184   Composition of the low-solidus component and effects on Na8

185

186   The effect of pyroxenite-derived melts on the final composition of the pooled MORB

187   depends upon the nature of the heterogeneities and on their dilution in the peridotite-

188   derived melt[17,30–32]. In mid-ocean ridge settings most pyroxenites produce melts with

189   major-element composition similar to those derived from peridotite[33]. Hence, little

190   reactivity is expected when pyroxenite-derived melts mix with mantle peridotite-derived

191   melts[34]. We thus explore the possible composition of pyroxenites dispersed in the VLS

192   mantle by considering mixing of silica-deficient (SD) and silica-enriched (SE) pyroxenite-

193   derived melts with peridotite-derived melts. In a Na_2O versus MgO diagram, young VLS

194   lavas plot at higher Na_2O content than the older ones (Supplementary Fig. S2). We assume

195   that the youngest VLS Na-rich lavas, i.e. those showing a degree of melting similar to that

196   of the associated peridotites, derive from melting of the VUM source defining a peridotite

197   primitive melt composition that matches the VUM average Na_8 and F% (Supplementary

198   Table S2). We then calculated mixing lines between the VUM primitive melt and

199   pyroxenitic-derived melts obtained experimentally at variable degrees of melting from

200   different sources (Supplementary Fig. S2-S3). Melt mixing affects the estimated Na_8, and

201   consequently the estimated apparent degree of melting, depending on the absolute Na

202   content and Mg/Na ratio of the added melt fraction (Supplementary Fig. S3). Inferred Na_8

203   and apparent F of the mixed compositions show that SE-derived melts do not reproduce

204   the observed variability for reasonable fractions and degrees of melting of the pyroxenitic-

205   derived components (Supplementary Fig. S3). Among the SD pyroxenites only those

206   having high Mg/Na ratios, as M7-16, match the VLS observed variability. It is worth

207   noting that the mixed melts matching the VLS data are those obtained at high F (F=65%),

208   a value close to those predicted by thermodynamics[13–15]. Based on these calculation the

209   VLS variability can be approximated by linear mixing of a VUM primitive melt with ca.

210   30% M7-16 type pyroxenite-derived melt.

211

212

213   Size and nature of mantle domains

214

215   An important result of thermodynamic modelling[13,14] is that the undercooling inferred

216   from F% decoupling occurs only for a composite source where a lower-T solidus

217   component is finely dispersed in a high-T-solidus host to ensure efficient heat diffusion.

218   Adopting the calibration of [13] for tabular heterogeneities limits their size to be < 1 km, a

219   dimension close to those estimated from seismic scatter (<10 km)[35]. Cryptic stripes of

220   comparable size (4 km) have been described at the SEIR[36] and modelled based on Nd-Hf

221   MORB variability by [37]. The compositional trend observed along the VLS suggests a

222   decreasing decoupling of the measured parameters. The lateral extension of the melting

223   region reaches 300 km in the spreading direction, ca. 70 km along axis[26]. A single large

224   heterogeneity in the older mantle section would have measured tens of km in width,

225   excluding efficient heat diffusion within the heterogeneity itself. We deduce that the older

226   mantle section contained a cluster of small, tabular, low-T solidus components as in Figure

227   2, decreasing in time from ca. 15% to 0% of the volume.

228   VLS basalts ^{143}Nd/^{144}Nd versus ^{208}Pb/^{206}Pb ratios duplicate one of the mixing trends

229   recognized in South Atlantic basalt suites[38,39] (Supplementary Fig. S4), suggesting that

230   those endmembers are ubiquitous in the sub-Atlantic mantle.

231   VLS glasses ^{143}Nd/^{144}Nd and ^{87}Sr/^{86}Sr ratios vary in a restricted range (0.51295-

232   0.51317 and 0.70258-0.70351 respectively, Fig. 1, S5, Online Methods); in contrast,

233   mantle peridotite clinopyroxenes display a large scatter (^{143}Nd/^{144}Nd: 0.512024-0.513616;

234   ^{87}Sr/^{86}Sr: 0.702220-0.705508, age corrected values). This different compositional scatter

235   can be generated by chromatographic dispersion in the melting column[40] or through time

236   by reactive melt infiltration and veining[41,42].

237   The VLS oldest basalts show the highest apparent degree of melting and the most

238   enriched Sr-Nd-Pb isotopic signature (Supplementary Fig. S4-S5). We suggest that their

239   compositions reflect a larger contribution of pyroxenite-derived melts. As a result, the

240   peridotites of the older domain are less affected by decompression melting, and record

241   lower degrees of melting, possibly preserving their original DMM isotopic fingerprint. In

242   contrast, the VLS younger basalts received a negligible contribution of pyroxenite-derived

243   melts. Unfortunately, we do not have enough data on the mantle peridotites of this young

244   VLS stretch because they are still buried below the sea floor; however the few available

245   samples indicate that this parcel of peridotitic mantle underwent high degree of melting.

246

247

248

249   Distribution of pyroxenites along Mid Ocean Ridges

250

251   We attempt now to extend our findings to other portions of the mid ocean ridge system

252   and interpret the chemistry of genetically related basalt/peridotite in terms of the

253   proportion of pyroxenite dispersed in the mantle source. Only two stretches of the global

254   MOR system have basalt-peridotite pairs sampled densely enough to allow first order

255   observations: the northern Mid Atlantic and the Southwest Indian Ridges[19,43]. In both cases

256   along axis mantle peridotites record an extent of melting systematically lower than that

257   recorded by the associated basalts (Fig. 4).

258   In light of our findings we propose that pyroxenites are widely distributed in subridge

259   mantle sources proportionally to $\Delta F_{\pi}^{\beta} = F_{\beta}^{app} - F_{\pi}$ the difference between the degree of

260   melting derived from basalts and that derived from peridotites (see Online Methods). This

8

261   interpretation, if correct, should be confirmed by a correlation between the extent of ΔF_{π}^{β}

262   and chemical indicators of the presence of pyroxenite in the source, e.g. the isotopic ratios

263   of radiogenic elements, expected to be enriched in recycled materials. A broad negative

264   correlation appears between the measured ΔF_{π}^{β} and the basalt ^{143}Nd/^{144}Nd ratios (Fig. 5,

265   Supplementary Table S4), suggesting the dependence of the Nd isotopic composition on

266   ΔF_{π}^{β} (r^2=0.53) and revealing similar enriching mechanisms in the two ridge systems.

267   Spreading rate and mantle potential temperature may not be the leading factors

268   affecting the composition of the extracted basalts and of the residual mantle: the relative

269   proportion of pyroxenites versus peridotites in the mantle source maybe more important. A

270   major implication is that at constant temperature a pulse of low-melting pyroxenite

271   entering the melting region may not lead to a pulse of magmatism because the increased

272   undercooling of the mantle shrinks the peridotitic melting region contrasting the increase

273   of instantaneous pyroxenite melt production.

274   Our results show that low-T melting heterogeneities dispersed in the mantle source

275   affect not only the composition of the extracted basaltic melts, but also the total extent of

276   melting, the volume of extracted melts, and consequently crustal thickness.

277

278

289

290   Author contributions

291   D.B. performed the modelling. A.C. analysed the samples. D.B. and A.C. processed the

292   geochemical data and wrote jointly the paper. E.B. provided the opportunity and support

293   for sea-expeditions and work. All the authors discussed the results and the interpretations.

294

295

296

297

References

299

1. Bonatti, E. *et al.* Mantle thermal pulses below the Mid-Atlantic Ridge and temporal variations in the formation of oceanic lithosphere. *Nature* **423,** 499–505 (2003).

2. Brunelli, D., Seyler, M., Cipriani, A., Ottolini, L. & Bonatti, E. Discontinuous Melt Extraction and Weak Refertilization of Mantle Peridotites at the Vema Lithospheric Section (Mid-Atlantic Ridge). *J. Petrol.* **47,** 745–771 (2006).

3. Bonatti, E. *et al.* Flexural uplift of a lithospheric slab near the Vema transform (Central Atlantic): Timing and mechanisms. *Earth Planet. Sci. Lett.* **240,** 642–655 (2005).

4. Cipriani, A., Bonatti, E., Brunelli, D. & Ligi, M. 26 million years of mantle upwelling below a segment of the Mid Atlantic Ridge: The Vema Lithospheric Section revisited. *Earth Planet. Sci. Lett.* **285,** 87–95 (2009).

5. Cipriani, A., Brueckner, H. K., Bonatti, E. & Brunelli, D. Oceanic crust generated by elusive parents: Sr and Nd isotopes in basalt-peridotite pairs from the Mid-Atlantic Ridge. *Geology* **32,** 657–660 (2004).

6. Cipriani, A. *et al.* A 19 to 17 Ma amagmatic extension event at the Mid-Atlantic Ridge: Ultramafic mylonites from the Vema Lithospheric Section. *Geochemistry Geophys. Geosystems* **10,** (2009).

7. Plank, T. & Langmuir, C. H. Effects of the melting regime on the composition of the oceanic crust. *J. Geophys. Res.* **97,** 19749–19770 (1992).

8. Klein, E. M. & Langmuir, C. H. Global correlations of ocean ridge basalt chemistry with axial depth and crustal thickness. *J. Geophys. Res.* **92,** 8089 (1987).

9. Dick, H. J. B. & Bullen, T. Chromian spinel as a petrogenetic indicator in abyssal and alpine-type peridotites and spatially associated lavas. *Contrib. to Mineral. Petrol.* **86,** 54–76 (1984).

10. Michael, P. J. & Bonatti, E. Peridotite composition from the North Atlantic: regional and tectonic variations and implications for partial melting. *Earth Planet. Sci. Lett.* **73,** 91–104 (1985).

11. Katz, R. F. & Weatherley, S. M. Consequences of mantle heterogeneity for melt extraction at mid-ocean ridges. *Earth Planet. Sci. Lett.* **335–336,** 226–237 (2012).

12. Weatherley, S. M. & Katz, R. F. Melting and channelized magmatic flow in chemically heterogeneous, upwelling mantle. *Geochemistry Geophys. Geosystems* **13,** Q0AC18 (2012).

13. Katz, R. F. & Rudge, J. F. The energetics of melting fertile heterogeneities within the depleted mantle. *Geochemistry Geophys. Geosystems* **12,** 1–22 (2011).

14. Phipps Morgan, J. Thermodynamics of pressure release melting of a veined plum pudding mantle. *Geochemistry Geophys. Geosystems* **2,** (2001).

15. Sleep, N. H. Tapping of Magmas from Ubiquitous Mantle Heterogeneities : An alternative to Mantle plumes? *J. Geophys. Res.* **89,** 10029–10041 (1984).

16. Ito, G. & Mahoney, J. J. Flow and melting of a heterogeneous mantle: 1. Method and importance to the geochemistry of ocean island and mid-ocean ridge basalts. *Earth Planet. Sci. Lett.* **230,** 29–46 (2005).

336   17.   Shorttle, O. Geochemical variability in MORB controlled by concurrent mixing and crystallisation.
337   *Earth Planet. Sci. Lett.* **424,** 1–14 (2015).

338   18.   Rudge, J. F., Maclennan, J. & Stracke, A. The geochemical consequences of mixing melts from a
339   heterogeneous mantle. *Geochim. Cosmochim. Acta* **114,** 112–143 (2013).

340   19.   Warren, J. M. Global Variations in Abyssal Peridotite Compositions. *Lithos* **248–251,** 193–219
341   (2016).

342   20.   Bown, J. W. & White, R. S. Variation with spreading rate of oceanic crustal thickness and
343   geochemistry. *Earth Planet. Sci. Lett.* **121,** 435–449 (1994).

344   21.   Cande, S. C., LaBrecque, J. L. & Haxby, W. F. Plate kinematics of the South Atlantic: Chron C34 To
345   Present. *J. Geophys. Res. Solid Earth* **93,** 13479–13492 (1988).

346   22.   Cande, S. C. & Kent, D. V. Revised calibration of the geomagnetic polarity timescale for the Late
347   Cretaceous and Cenozoic. *J. Geophys. Res. Solid Earth* **100,** 6093–6095 (1995).

348   23.   Langmuir, C. H., Klein, E. M. & Plank, T. in *Mantle Flow and Melt Generation at Mid-Ocean*
349   *Ridges* (ed. Morgan, J. P.) 183–280 (American Geophysical Union, 1992).

350   24.   Lambart, S., Baker, M. B. & Stolper, E. M. The role of pyroxenite in basalt genesis: Melt-PX, a
351   melting parameterization for mantle pyroxenites between 0.9 and 5 GPa. *J. Geophys. Res. Solid*
352   *Earth* **121,** 0–28 (2016).

353   25.   Shorttle, O. & Maclennan, J. Compositional trends of Icelandic basalts: Implications for short-length
354   scale lithological heterogeneity in mantle plumes. *Geochemistry, Geophys. Geosystems* **12,** (2011).

355   26.   Ligi, M., Cuffaro, M., Chierici, F. & Calafato, A. Three-dimensional passive mantle flow beneath
356   mid-ocean ridges: an analytical approach. *Geophys. J. Int.* **175,** 783–805 (2008).

357   27.   Mckenzie, D. & Bickle, M. J. The volume and composition of melt generated by extension of the
358   lithosphere. *J. Petrol.* **29,** 625–679 (1988).

359   28.   Shen, Y. & Forsyth, D. W. Geochemical constraints on initial and final depths of melting beneath
360   mid-ocean ridges. *J. Geophys. Res.* **100,** 2211–2237 (1995).

361   29.   Lambart, S., Laporte, D. & Schiano, P. Markers of the pyroxenite contribution in the major-element
362   compositions of oceanic basalts: Review of the experimental constraints. *Lithos* **160–161,** 14–36
363   (2013).

364   30.   Stracke, A., Bourdon, B. & McKenzie, D. Melt extraction in the Earth's mantle: Constraints from U-
365   Th-Pa-Ra studies in oceanic basalts. *Earth Planet. Sci. Lett.* **244,** 97–112 (2006).

366   31.   Stracke, A. & Bourdon, B. The importance of melt extraction for tracing mantle heterogeneity.
367   *Geochim. Cosmochim. Acta* **73,** 218–238 (2009).

368   32.   Rubin, K. H., Sinton, J. M., Maclennan, J. & Hellebrand, E. Magmatic filtering of mantle
369   compositions at mid-ocean-ridge volcanoes. *Nat. Geosci.* **2,** 321–328 (2009).

370   33.   Lambart, S., Laporte, D. & Schiano, P. An experimental study of pyroxenite partial melts at 1 and
371   1.5GPa: Implications for the major-element composition of Mid-Ocean Ridge Basalts. *Earth Planet.*
372   *Sci. Lett.* **288,** 335–347 (2009).

373   34.   Lambart, S., Laporte, D., Provost, a. & Schiano, P. Fate of Pyroxenite-derived Melts in the
374   Peridotitic Mantle: Thermodynamic and Experimental Constraints. *J. Petrol.* **53,** 451–476 (2012).

375   35.   Helffrich, G. R. & Wood, B. J. The Earth's mantle. *Nature* **412,** 501–7 (2001).

376 36. Graham, D. W., Blichert-Toft, J., Russo, C. J., Rubin, K. H. & Albarede, F. Cryptic striations in the
377   upper mantle revealed by hafnium isotopes in southeast Indian ridge basalts. *Nature* **440,** 199–202
378   (2006).

379 37. Liu, B. & Liang, Y. The prevalence of kilometer-scale heterogeneity in the source region of MORB
380   upper mantle. 1–8 (2017).

381 38. Hoernle, K. *et al.* On- and off-axis chemical heterogeneities along the South Atlantic Mid-Ocean-
382   Ridge (5-11°S): Shallow or deep recycling of ocean crust and/or intraplate volcanism? *Earth Planet.*
383   *Sci. Lett.* **306,** 86–97 (2011).

384 39. Paulick, H., Münker, C. & Schuth, S. The influence of small-scale mantle heterogeneities on Mid-
385   Ocean Ridge volcanism: Evidence from the southern Mid-Atlantic Ridge (7°30′S to 11°30′S) and
386   Ascension Island. *Earth Planet. Sci. Lett.* **296,** 299–310 (2010).

387 40. Liang, Y. Simple models for dynamic melting in an upwelling heterogeneous mantle column:
388   Analytical solutions. *Geochim. Cosmochim. Acta* **72,** 3804–3821 (2008).

389 41. Borghini, G. *et al.* Meter-scale Nd isotopic heterogeneity in pyroxenite-bearing Ligurian peridotites
390   encompasses global-scale upper mantle variability. *Geology* **41,** 1055–1058 (2013).

391 42. Borghini, G. *et al.* Pyroxenite Layers in the Northern Apennines' Upper Mantle (Italy)—Generation
392   by Pyroxenite Melting and Melt Infiltration. *J. Petrol.* **57,** 625–653 (2016).

393 43. Gale, A., Langmuir, C. H. & Dalton, C. A. The global systematics of ocean ridge basalts and their
394   origin. *J. Petrol.* **55,** 1051–1082 (2014).

395

396

397

Figure captions

399

Figure 1: Figure 1. a) Temporal variation of the VLS basaltic glasses $^{143}Nd/^{144}Nd$ isotopic ratios. Solid circles define three domains (average Nd isotopic ratio of each sector is indicated). Dashed line is average of oldest sector without one enriched sample.

b) Temporal variation of the degree of melting as inferred by mantle peridotite residues[19] and erupted MORBs[7]. Each point represents a dredge average. Thick bold lines are linear regressions; thin lines show 95% confidence bands. The age of mantle rocks is corrected for the time lag between their arrival at the seafloor and the arrival of the basaltic melts they produced according to [1,4] (see Methods).

408

409

Figure 2: Interpretative sketch of the upwelling mantle column below the Vema Lithospheric Section. At constant mantle potential temperature the presence of pyroxenites causes a contraction of the melting region. Total degree of decompressive adiabatic melting is computed based on Melt-PX algorithm[24]. In the older VLS sectors, the onset of melting of the mantle peridotite is delayed and its degree of melting reduced (F_{max}=8). The associated pyroxenite melts more (F_{max}=53) and contributes to the higher apparent degree of melting in the pooled MORBs. Undercooling of the mantle peridotite causes deepening of the end of the melting column estimated to shallow by 0.4 GPa from the older to the younger sector.

419

420

Figure 3: Melt-PX[24] numerical experiments for adiabatic melting of a two-component mantle source: lherzolite plus SD pyroxenite (M7-16[29]). The thick black line represents the model limit value for melting ceasing at the base of the crust.

Left Panel: the degree of melting of the host peridotite is lowered by adding up to 40% pyroxenite in the source. Variable extents of the melting column are computed assuming P_f from 1.1 to 0.3 GPa. Red dashed lines correspond to the VLS average melting interval from old (F_{max}=8.0) to young (F_{max}=14.2) sectors.

428   Panel B: Variation of the aggregated crustal thickness as function of pyroxenite fraction

429   in the source and final depth of melting. Average values for the VLS extremes are plotted

430   as red symbols and 1σ standard deviation

431

432   **Figure 4**: Variation of the degree of melting estimated from mantle peridotite (blue

433   dots) and associated basalts (red dots) along the Southwest Indian Ridge (upper) and the

434   Mid Atlantic Ridge from the Equator to the Azores hotspot region (lower). Degrees of

435   melting are calculated based on [19,23,43] on data compiled from PetDB

436   (www.earthchem.org/petdb). Variations of the amount of low-T melting heterogeneities

437   (pyroxenite) in the source result in larger differences in the estimated degree of melting

438   (ΔF_π^β), a proxy for the along axis pyroxenite vol% content of the source.

439

440   **Figure 5**: Difference of degree of melting estimated from genetically related basalts and

441   peridotites (ΔF) versus the Nd isotopic composition of basalt. The VLS sectors are plotted

442   as large red circles; delta F increases from sector 1 to 3 (young to old). Black diamonds

443   represent SWIR, blue circles MAR. Regression lines are calculated for the whole

444   population (red solid line), the SWIR (black solid line) and the MAR (blue solid line).

445   Data and parameters in supplementary Table S4; 95% confidence bands are plotted in

446   Supplementary Fig. S6. Our interpretation is that the ΔF between basalt and peridotite is a

447   proxy of the amount of low-T solidus pyroxenites in the source.

448

449

METHODS

451

Analytical Methods

453 Major elements
454 Major elements on mineral phases were collected with the electron probe (Cameca SX100)
455 at the American Museum of Natural History (NY) using 15kV acceleration voltage, 20nA
456 beam, a 10μm diameter beam and 30 s counting times. Sodium, potassium and chlorine
457 were run under different conditions to attain a higher precision and monitor their mobility,
458 with a 5nA beam and counting times of 80 s. A subset of samples has been analyses with a
459 Cameca X-Five microprobe at the CAMPARIS micro-analytical center (University of
460 Paris VI), following procedures detailed in [44]. A number of primary mineral standards
461 were used, as well as the MORB JDF-D2 standard.

462 Isotope ratios
463 For isotopic determinations 50 to 250 mg of basaltic glass and clinopyroxene separate
464 were prepared by grinding, sieving and handpicking under a binocular microscope. Glass
465 chips were leached in 8N HNO_3. Clinopyroxenes were treated with three leachates to
466 eliminate the effects of seawater alteration[5,45]. Pb was separated using AG1-X8 anion
467 resin, Sr was separated using Eichrom Sr resin and Nd was separated in a two-column
468 procedure using Eichrom TRU-spec resin to separate the rare-earth elements, followed by
469 α-hydroxy isobutyric acid. Isotopes were measured on a VG Sector 54 multicollector mass
470 spectrometer housed at the Lamont Doherty Earth Observatory of Columbia University. Sr
471 and Nd isotopes were measured in multidynamic mode. The mass fractionation corrections
472 were based on $^{86}Sr/^{88}Sr = 0.1194$ and $^{146}Nd/^{144}Nd = 0.7219$. Over the period of analytical
473 work, repeated analyses yielded a $^{87}Sr/^{86}Sr$ ratio of 0.710271 ± 0.000015 for the NBS-987
474 Sr standard (2σ external reproducibility, n>22) and a $^{143}Nd/^{144}Nd$ ratio of $0.512096 \pm$
475 0.000023 for the JNdi-1 (2σ external reproducibility, n>38). Total blanks for Sr and Nd did
476 not exceed 80pg. Pb data on basaltic glasses were collected in static mode, using the
477 double spike technique with the calibrated 207/204 spike. Replicate analyses of the Pb
478 isotope standard NBS981 gave an average of 16.9317±0.0022 and 15.4912±0.0027 and
479 36.7060±0.0066 for $^{206}Pb/^{204}Pb$, $^{207}Pb/^{204}Pb$, and $^{208}Pb/^{204}Pb$, respectively. These measured
480 Pb isotope ratios were corrected to the values defined by [46] of 16.9356, 15.4891, and
481 36.7006, respectively, for NBS 981. Reproducibility for NBS981 is 130, 174, and 181 ppm
482 (2σ, N=47), for $^{206}Pb/^{204}Pb$, $^{207}Pb/^{204}Pb$, and $^{208}Pb/^{204}Pb$ ratios, respectively. Pb blanks
483 measured were below 100pg and thus negligible relative to the amount of sample analysed.

484

Estimate of the ΔF_{π}^{β} and $^{143}Nd/^{144}Nd$ of the associated basalts

486 Figure 4 of the main text reports the correlation between ΔF_{π}^{β}, as the differential in degree
487 of melting between basalt and peridotites, and the Nd isotopic composition of basalts of
488 several portions of the Mid Ocean Ridge system where both basalts and peridotites have

489 been sampled. Among all the explored ridge segments, only few localities report basalts
490 and mantle peridotites sampled in the same dredge haul or site. Basaltic rocks are generally
491 more abundant and present a much denser lateral sampling than mantle peridotites. Basalt
492 chemistry and isotopic ratios appear to vary systematically over variable length scale
493 defining domains in which they show little variability or monotonic changes along the
494 ridge axis (e.g. [43, 47-48] among others). Domains characterized by reduced variability of the
495 chemical character of the basalts are usually bounded by major transform faults, which
496 also act as thermal barriers[47,49-51]. Therefore, in Figure 4 (main text), we have chosen to
497 integrate the dataset of the sites where peridotites and basalts were sampled together with
498 sites where only mantle rocks were recovered, but for which is possible to infer the
499 isotopic composition of the associated basalts from the regional variability. As a
500 conservative approach, we only considered those domains in which lateral isotopic and
501 compositional variability is very low or described by simple monotonic trends.
502 The degree of melting of mantle-peridotites can be affected by Cr# fluctuations due to
503 melt/rock interaction that modify spinel[9] and pyroxene compositions[52]. Therefore we
504 filtered spinel composition and applied a threshold of $TiO_2 < 0.15$ wt% as discussed in [2,19].
505 The supplementary Table S4, reports the inferred values showing the measured and
506 calculated value for each basalt-peridotite couple. The "regional regression" data are
507 calculated considering sets of neighboring peridotites and basalts, whereas the "local
508 average" set of data refers to basalts and peridotites sampled from the same site. $\pm\sigma$ on
509 ΔF_{π}^{β} are estimated by error propagation.

510

Age correction

512 Basalts from the VLS were erupted over a time range of 26 Ma. We applied, hence, an age
513 correction for radiogenic ingrowth since the closure of the system to allow comparisons of
514 their initial isotopic composition, which is controlled only by the source. The correction
515 time should be calculated since the closure of the system, represented by the moment of
516 separation between the source and the melt at depth, assuming there was no significant
517 melt-rock interaction thereafter. This is attested by mantle residual rocks from the VLS
518 being all equilibrated in the spinel field showing no late interaction with melts. The only
519 report of plagioclase-equilibrated mantle rocks concerns the strain-driven formation of
520 plagioclase in fertile lherzolites during mylonitization[53]. We identify the melt-source
521 separation at the estimated upper limit of melting as inferred by modelling with Melt-PX
522 (see main text).
523 Based on the estimation of melting a composite source and varying the position of the end
524 of the melting column between 1.2 and 0.3 GPa, it appears that the end of the melting
525 column can be constrained based on the correlation with the measured crustal thickness
526 and degree of melting of the residual mantle. For the time stretch relative to the VLS the
527 end of the melting column can be set at 1.1 GPa for the older domain and 0.7 GPa for the
528 younger domain. Based on Africa-South America Euler vectors of [21] and the geomagnetic
529 time scale of [22], the spreading rate at the EMAR axis can be estimated through time. As
530 shown in Figure 1 of the main text, the spreading rate decreased steadily in the last 30 Ma.
531 The absolute value decreases from 17.2 to 16.9 mm/y at Chron 6 (half spreading rate) and

532   from 16.9 to 13.6 mm/y at Chron 5. Crustal ages can be calculated accordingly during this

533   time stretch assuming basalts erupted in the axial region.

534   Times of extraction for the mantle residue and for the basalts are, however, very different.

535   Ascent rates for the basaltic liquids are estimated in the range of m/y [54-56]. Setting the

536   melt/source separation at 1.1 and 0.7 GPa and upwelling rates in the range 1-5 m/y [56] gives

537   upwelling times ranging 7-36 ka for the older VLS domain and 5-23 ka for the younger

538   VLS domain. Such delays are uninfluential in the age correction of long-time decay

539   systems as those here discussed (Sm-Nd; Rb-Sr; U-Pb); however, we considered this

540   contribution for the total age correction when discussing age corrected values in Figs 1B

541   and S1.

542   Upwelling of the mantle lasts a significant amount of time and can sensibly modify the

543   isotopic relationships. The time necessary for a mantle parcel to join the crust from the end

544   of melting depth is 2.1 Ma for the older VLS domain and 1.7 Ma for the younger VLS

545   domain.

546

547

548

549

550

References

44. Seyler, M. & Brunelli, D. Sodium chromium covariation in residual clinopyroxenes from abyssal peridotites sampled in the 43°–46°E region of the Southwest Indian Ridge. *Lithos* **302–303,** 142–157 (2018).

45. Cipriani, A., Bonatti, E. & Carlson, R. W. Nonchondritic [142]Nd in suboceanic mantle peridotites. *Geochemistry, Geophys. Geosystems* **12,** 1–8 (2011).

46. Todt, W., Cliff, R., Hanser, A. & Hofmann, A. W. Evaluation of a 202Pb–205Pb double spike for high - precision lead isotope analysis. *Geophys. Monogr. Ser.* **95,** 429–437 (1996).

47. Meyzen, C. M. *et al.* New insights into the origin and distribution of the DUPAL isotope anomaly in the Indian Ocean mantle from MORB of the Southwest Indian Ridge. *Geochem. Geophys. Geosyst.* **6,** Q11K11 (2005).

48. Meyzen, C. M., Toplis, M. J., Humler, E., Ludden, J. N. & Mevel, C. A discontinuity in mantle composition beneath the southwest Indian ridge. *Nature* **421,** 731–733 (2003).

49. Cannat, M., Rommevaux-Jestin, C., Sauter, D., Deplus, C. & Mendel, V. Formation of the axial relief at the very slow spreading Southwest Indian Ridge (49° to 69°E). *J. Geophys. Res.* **104,** 22825–22843 (1999).

50. Seyler, M., Brunelli, D., Toplis, M. J. & Mével, C. Multiscale chemical heterogeneities beneath the eastern Southwest Indian Ridge (52°E-68°E): Trace element compositions of along-axis dredged peridotites. *Geochemistry, Geophys. Geosystems* **12,** (2012).

51. Paquet, M., Cannat, M., Brunelli, D., Hamelin, C. & Humler, E. Effect of melt/mantle interactions on MORB chemistry at the easternmost Southwest Indian Ridge (61°–67°E). *Geochemistry, Geophys. Geosystems* **17,** (2016).

52. Brunelli, D., Paganelli, E. & Seyler, M. Percolation of enriched melts during incremental open-system melting in the spinel field: A REE approach to abyssal peridotites from the Southwest Indian Ridge. *Geochim. Cosmochim. Acta* **127,** 190–203 (2014).

53. Cannat, M. & Seyler, M. Transform tectonics, metamorphic plagioclase and amphibolitization in ultramafic rocks of the Vema transform fault (Atlantic Ocean). *Earth Planet. Sci. Lett.* **133,** 283–298 (1995).

54. Spiegelman, M. & Kenyon, P. The requirements for chemical disequilibrium during magma migration. *Earth Planet. Sci. Lett.* **109,** 611–620 (1992).

55. Spiegelman, M. & Elliott, T. Consequences of melt transport for uranium series disequilibrium in young lavas. *Earth Planet. Sci. Lett.* **118,** 1–20 (1993).

56. Lundstrom, C. C., Gill, J., Williams, Q. & Perfit, M. R. Mantle Melting and Basalt Extraction by Equilibrium Porous Flow. *Science (80-.).* **270,** 1958 LP-1961 (1995).
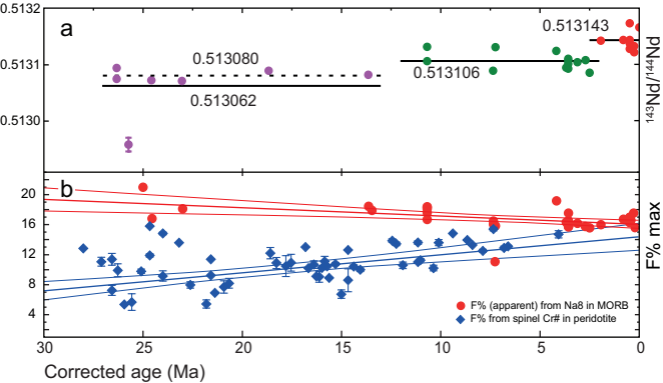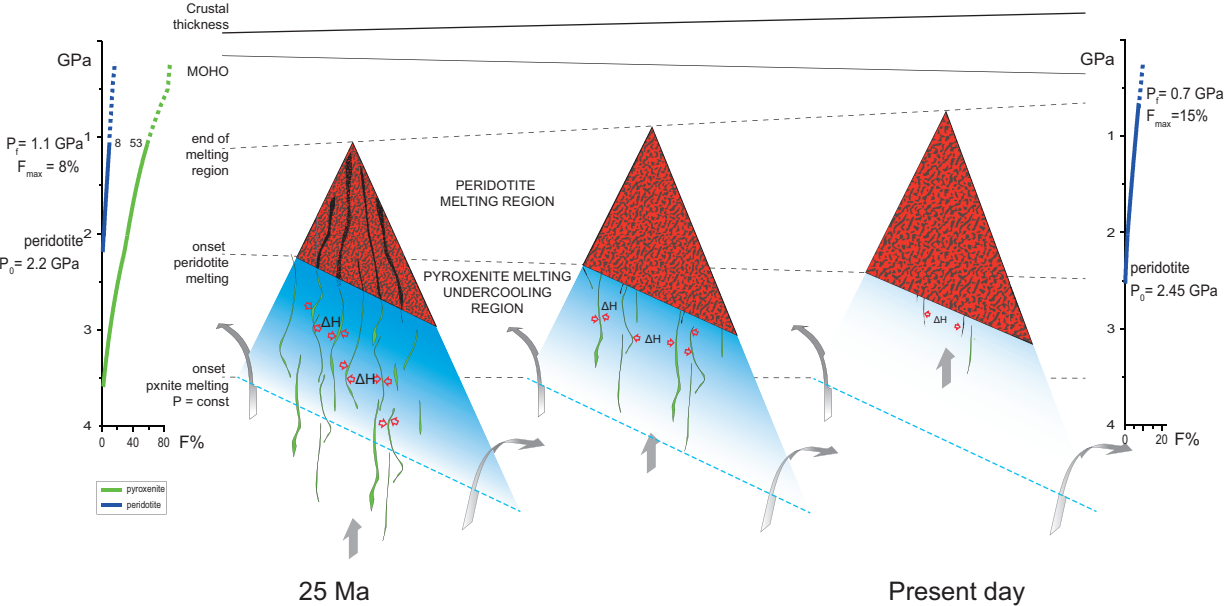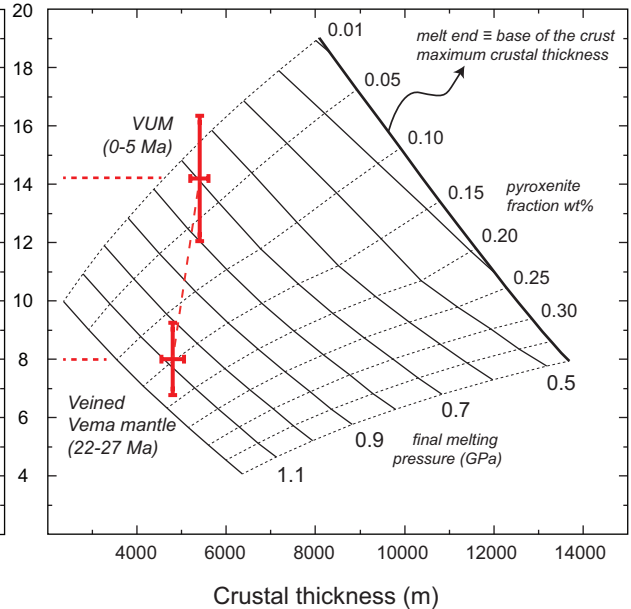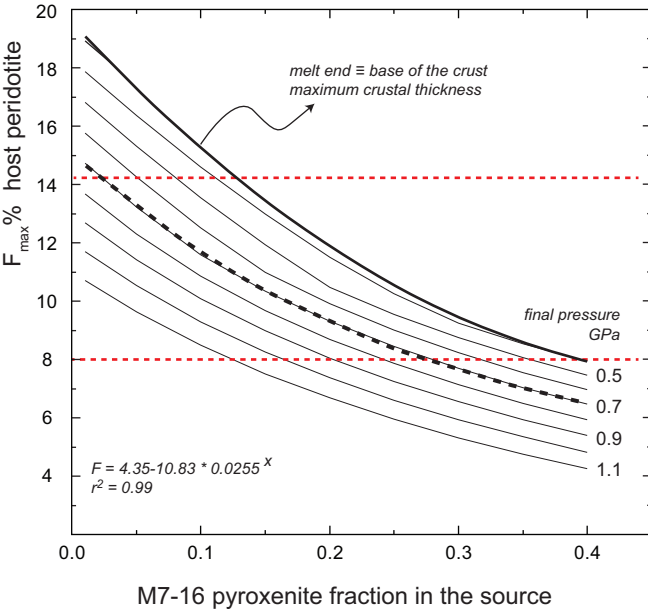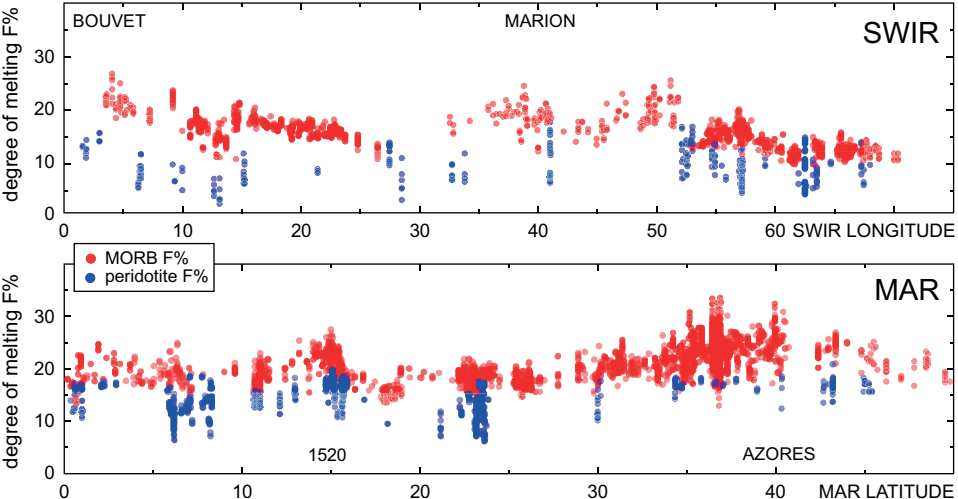
Fig. 1

Figure 2 - last

Figure 3_last

Figure 4-last

Figure 5 - last